






PHOTONICS Research

Large-scale error-tolerant programmable interferometer fabricated by femtosecond laser writing

ILYA KONDRATYEV,^{1,*}  VERONIKA IVANOVA,² SUREN FLDZHYAN,^{1,2}  ARTEM ARGENCHIEV,¹ NIKITA KOSTYUCHENKO,¹ SERGEY ZHURAVITSKII,¹ NIKOLAY SKRYABIN,¹  IVAN DYAKONOV,^{1,2}  MIKHAIL SAYGIN,^{1,3} STANISLAV STRAUPE,^{1,2}  ALEXANDER KORNEEV,¹ AND SERGEI KULIK^{1,3}

¹Quantum Technology Centre and Faculty of Physics, M. V. Lomonosov Moscow State University, Moscow 119991, Russia

²Russian Quantum Center, Moscow 121205, Russia

³Laboratory of Quantum Engineering of Light, South Ural State University, Chelyabinsk 454080, Russia

*Corresponding author: iv.kondratjev@physics.msu.ru

Received 3 October 2023; revised 16 December 2023; accepted 2 January 2024; posted 16 January 2024 (Doc. ID 504588); published 1 March 2024

We introduce a programmable eight-port interferometer with the recently proposed error-tolerant architecture capable of performing a broad class of transformations. The interferometer has been fabricated with femtosecond laser writing, and it is the largest programmable interferometer of this kind to date. We have demonstrated its advantageous error tolerance by showing an operation in a broad wavelength range from 920 to 980 nm, which is particularly relevant for quantum photonics due to efficient photon sources existing in this wavelength range. Our work highlights the importance of developing novel architectures of programmable photonics for information processing. © 2024 Chinese Laser Press

<https://doi.org/10.1364/PRJ.504588>

1. INTRODUCTION

Programmable multiport interferometers (PMIs) are targeted at precise, energy-efficient, and compact manipulation of information encoded in multiple modes of optical fields [1,2]. The growing interest in PMIs is fueled by a significant number of applications: optical switching in telecommunications [3–5], matrix-vector multiplication in optical neural networks [6,7], and quantum information processing [8–10]. Broadband operation [11] and low power consumption [12] are two special features that are driving the growing interest of the scientific community and industry in information processing with PMIs.

A PMI is a static waveguide structure endowed with tunable phaseshifters (PSs). In N -port PMIs, a phase pattern induced by a set of PSs programs a specific $N \times N$ unitary transformation matrix U , which should be applied to an input vector of light field amplitudes. The PMI architecture can be either dictated by a particular task [10,13] or represent a general class of PMIs often called universal photonic processors. A universal photonic processor provides access to a full space of unitary transformations of input light vectors, and the transformation $U(\{\phi\})$ is precisely controlled by phases $\{\phi\}$. Conventional universal photonic processor architectures rely on a well-known

unitary matrix decomposition into a sequence of two-dimensional subspace rotations [14,15]. Each subspace rotation can be implemented using a Mach–Zehnder interferometer (MZI) acting on a particular pair of modes belonging to a chosen subspace. Each MZI matrix $U_{\text{MZI}}(\theta, \phi)$ is essentially a 2×2 variable beamsplitter matrix embedded in a larger $N \times N$ unitary of a complete PMI. Such PMI architectures are particularly appealing due to the existence of an analytical algorithm that computes phase sets $\{\theta\}$ and $\{\phi\}$ corresponding to a desired PMI unitary matrix U . The universality of these architectures hinges on the ability of an ideal MZI to cover the entire $SU(2)$ group, which implies that the static beamsplitters (BSs) constituting the MZIs must be ideally balanced. However, nonperfect manufacturing quality of the static elements hinders the universality of the fabricated PMIs. State-of-the-art technology and design tools deal with the majority of problems providing wafer-scale fabrication of high-quality components [16], which are engineered to be robust [17]. However, errors still may creep once truly large-scale interferometers are fabricated [18] and may even evolve during long-term operation.

Therefore, developing more advanced interferometer architectures that would tolerate high levels of static errors is paramount and could facilitate the creation of sophisticated

photonic processors. Several works have studied usage of alternative building blocks as a foundation of robust architectures instead of MZIs, in particular, BSs and multiport couplers [17,19]. It turns out that specific arrangements of these devices and phaseshifting elements can lead to architectures that tolerate large deviations of their static elements from ideal counterparts, which relaxes the requirements to fabrication tolerances and expands the range of possible applications. For instance, since the unitary matrix of both the BS and the multiport coupler is susceptible to a signal wavelength, the PMI with a robust architecture can work as a more broadband optical processor than the MZI-based one, which, in its turn, may also support broadband operation by careful engineering of its static components [20]; however, this step usually complicates both development and fabrication processes and results in the increasing overall size of the interferometer [20,21].

The state-of-the-art PMI fabrication technology is a lithography-based process [22], which offers compatibility with the standard CMOS production line [23]. This approach provides both flexible and extremely precise tools for the fabrication of nano- and microscale photonic structures. The largest PMIs to date were fabricated using lithography-based Triplex technology [24]. The quality of the fabricated PMIs can be estimated either by comparing an implemented unitary transformation with a desired counterpart [25], which is a tedious procedure, or by running a specific task and checking the device performance. For instance, a deep interest in PMIs grows from their natural ability to multiply an input complex field vector by a unitary matrix. Hence the quality may be assessed by checking the precision of this operation. This method has found wider application in PMI quality estimation [26]. Tests using both methods indicate that lithographically fabricated processors can be of very high quality [9]. In this work we use an alternative fabrication technology—femtosecond laser writing (FSLW)—that can be used for rapid and cost-effective PMI prototyping [27]. It has been widely adopted by the scientific community not only due to its relative simplicity and potential to produce PMIs with competitive quality, but also since it has a feature to fabricate waveguide structures in three dimensions in comparison with the lithography-based process whose waveguide geometries are inherently planar [28–30]. Recently, a six-port universal MZI-based PMI fabricated by FSLW with 30 thermo-optical modulators was reported [31]. On the other hand, the FSLW technology offers less precision and PMIs suffer from substantially larger crosstalks between PSs [32]. Therefore, this technology should benefit especially from robust architectures. Regardless of the technological platform, robust architecture can significantly improve PMI quality, making it a universal method for error-prone optical multiport design.

In this paper, we demonstrate an eight-port PMI based on the error-tolerant architecture [19]. The interferometer is fabricated using FSLW technology and includes 56 directional couplers (DCs) and 56 thermo-optical PSs. To the best of our knowledge, this is the largest PMI that has been fabricated using FSLW to date. We demonstrate broadband port-to-port switching by tuning the interferometer with an optimization procedure. The reported result indicates that the error-tolerant

architecture adds robustness even to PMIs that are fabricated with less stringent technological processes.

2. METHODS

A. Interferometer Fabrication

The studied eight-port PMI was fabricated by the FSLW technique in a fused silica glass (JGS1, AGOptics) sample with the size of 100 mm × 50 mm × 5 mm (see Appendix A for details). The waveguide architecture of the PMI is shown in Fig. 1 with the input and output ports to be separated by a 127 μm gap to interface with v-groove single-mode fiber arrays. The DC design includes a pair of waveguides with two circular arc s-bends with 60 mm radius and a minimum distance d between the waveguide cores. The PSs are implemented as thin metallic wires, which induce refractive index change due to the thermo-optical effect. The NiCr film with a thickness of about 0.2 μm is deposited on the top surface of the optical chip by a magnetron sputtering process. The heating wires and contact pads are engraved by laser ablation using the same FSLW setup. The geometric parameters of the heating wires are adjusted such that their typical resistances are around $R_b = 450 \Omega$ (see Appendix B for details).

As the key component of our PMI is a directional coupler (DC), its parameters were carefully calibrated. A generic DC is completely described with a 2×2 unitary matrix $U_{DC} = \begin{pmatrix} \sqrt{1-T} & i\sqrt{T} \\ i\sqrt{T} & \sqrt{1-T} \end{pmatrix}$, where T is the power transmission coefficient. In order to select the appropriate parameters of the DCs, a series of 11 DCs with varying distances d was fabricated. The distance d was set within the range of 5.5–8.5 μm with a step of 0.3 μm. The transmission coefficient T was measured for each DC in the wavelength range from 910 to 980 nm with a step of 10 nm. The results are shown in Fig. 2. The error-tolerant interferometer architecture described in Ref. [19] requires the transmission coefficients of the DCs to be in the range 0.5–0.8. The data in Fig. 2 suggest that DCs with $7.5 \mu\text{m} < d < 8 \mu\text{m}$ satisfy this requirement, and $d = 7.8 \mu\text{m}$ was chosen for the fabricated PMIs.

To verify the reproducibility of a single DC in our FSLW setup, 40 DCs with $d = 7.8 \mu\text{m}$ were fabricated, and the corresponding transmission coefficients T were measured. The values obtained are shown in Fig. 3. It can be seen that, while values of T underwent noticeable fluctuations, the transmission coefficients were still in the required range 0.5–0.8 for all 40 DCs, which is necessary for the architecture of our interferometer to preserve its universality.

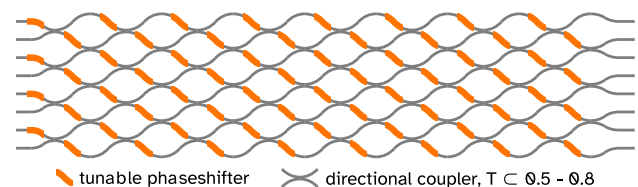


Fig. 1. Scheme of an eight-port error-tolerant interferometer architecture that consists 56 DCs and 56 tunable PSs. Each DC has an imbalanced splitting ratio shifted to a higher transmission 0.5–0.8 according to original proposal [19].

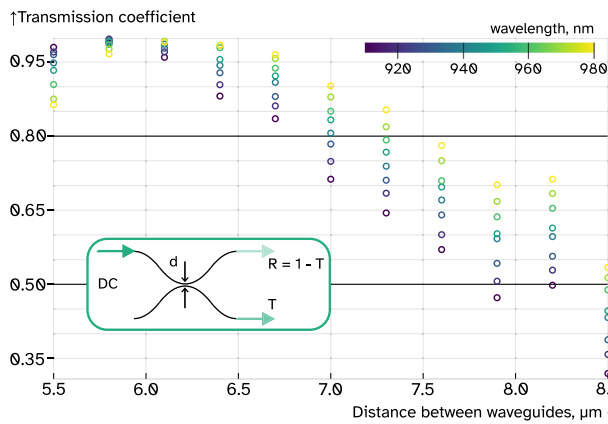


Fig. 2. Dependence of the transmission coefficients on the distance between the waveguides in the DC at different wavelengths. The black solid lines limit the transmittance range 0.5–0.8 that is required by the PMI architecture [19]. Inset schematically shows the DC structure.

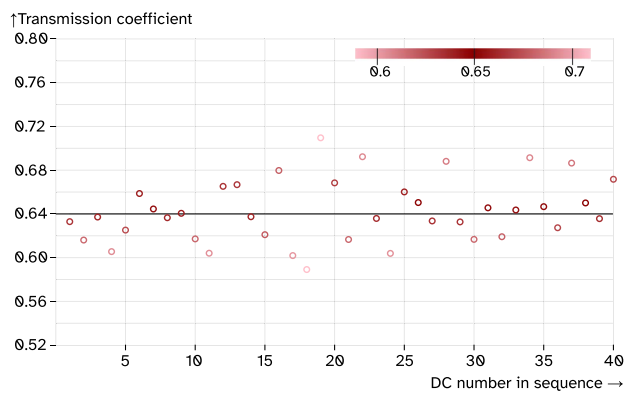


Fig. 3. Statistics of the transmission coefficient for 40 DCs with $d = 7.8 \mu\text{m}$ at the 945 nm wavelength. Noticeable fluctuations in the absolute value of the transmission coefficient T are clearly visible. However, T falls in the required range 0.5–0.8 for all 40 directional couplers.

B. Experimental Setup

The general experiment setup is sketched in Fig. 4 having in its core the eight-port PMI. Input and output fiber arrays are connected to the tunable CW diode laser (Toptica CTL 950) and eight photodetectors, respectively. The polarization of the input radiation was controlled by the HWP and QWP installed in the

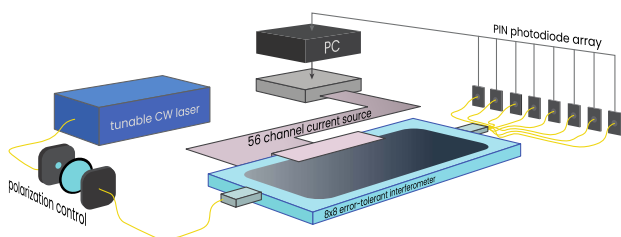


Fig. 4. Sketch of the experimental setup. The PMI was connected to a 64 channel current source capable of setting currents up to 60 mA in each of its channels individually with a step of 0.01 mA. The current source was connected to and fully controlled from a PC.

free-space area before the input fiber array. A home-built 12-bit digital constant current source powers the heaters, and a specific printed circuit board with spring-loaded connectors interfaces the PMI with the current source. The optical chip was mounted on a temperature stabilized aluminum platform with a temperature setpoint around 20°C.

3. EXPERIMENT AND RESULTS

We tested the fabricated PMI by programming it to operate as an 8×8 optical port-to-port switch at three different wavelengths: 920, 945, and 980 nm. At each wavelength, the DC structures inside the PMI are characterized by a corresponding transmission coefficient (see Fig. 2), and thus we tested the performance of the error-tolerant architecture within the required transmission range of 0.5–0.8. It is noteworthy that optical port-to-port switching is a particularly difficult task for an MZI-based universal interferometer since perfect switching can only be achieved when the DC transmission T is exactly 0.5 or an optimization routine has to be introduced in order to minimize the effect of nonperfect DC. We present a numerical comparison of switching performance of both error-tolerant and MZI-based architectures by varying the identical transmission coefficients for all the DCs in Fig. 5. Figure 5 demonstrates the regions of transmission coefficients, which support perfect port-to-port switching for a particular input port of the 8×8 PMI based on either conventional MZI architecture or error-tolerant architecture. The details of the simulation and additional analysis are provided in Appendix C. It is clearly evident from Fig. 5 that the error-tolerant architecture is substantially more robust to the DC transmission coefficient variations as it has significantly wider regions of transmission coefficients allowing for perfect port-to-port switching for each input port.

We experimentally program our PMI to implement switching configurations using a global optimization routine. To do this we conducted a series of optimization experiments by reconfiguring the chip to switch one-to-one all optical power

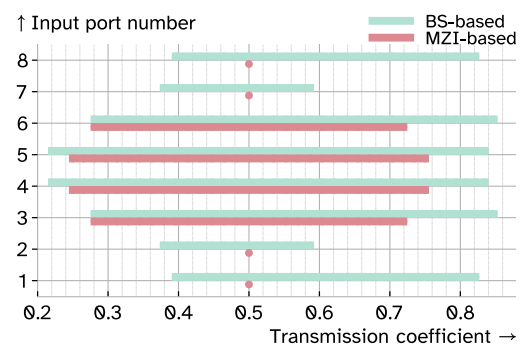


Fig. 5. Simulated numerical comparison of the performance of realizing port-to-port optical mode switching between BS-based error-tolerant PMI [19] and conventional MZI-based PMI [15] architectures. The colored regions show the transmissions of all the DCs of switching-capable PMI configurations. The PMI was considered capable of realizing the switching task if the optimization procedure converged to the infidelity values lower than 10^{-3} for switching to each of eight output ports from the particular input port. If the PMI comprising DCs with transmission coefficients T satisfied the criterion (for a particular input mode), a colored marker was put on the plot.

from each of the first four input ports to each of the eight output ports as is schematically shown in Fig. 6(a). The optimizer searches for the 56 phase values inside the interferometer that correspond to the desired output power distribution. We use a very fast simulated annealing (VFSA) algorithm [33] to minimize the infidelity $\text{Inf} = 1 - F$ with the fidelity function defined as

$$F(X, Y) = \left(\sum_j \sqrt{X_j Y_j} \right)^2, \quad (1)$$

where X and Y are the normalized column vectors ($\sum X_j = \sum Y_j = 1$) corresponding to the experimentally measured and target output power distributions, respectively.

The experimental results are shown in Fig. 6(b). Each row of the bar charts illustrates the results of output power

measurements from the optical chip optimized to realize a given configuration. The colors of the histograms encode the wavelength used in the experiment (red color, 920 nm; orange, 945 nm; yellow, 980 nm). The right column shows the fidelity values for each optimized output distribution after 500 iterations of the optimization algorithm. The convergence curves are provided in Appendix D. The average switching fidelities for all input ports and wavelengths are in the range between 0.89 and 0.93. The results provide clear evidence that the PMI constructed using a BS-based robust architecture is capable of high-performance switching when the static DCs' transmissions lie in the 0.5–0.8 range.

During the optimization process, the temperatures of the PSs were adjusted stepwise with a 10 s delay between the steps to maintain a constant chip temperature of 20°C. The

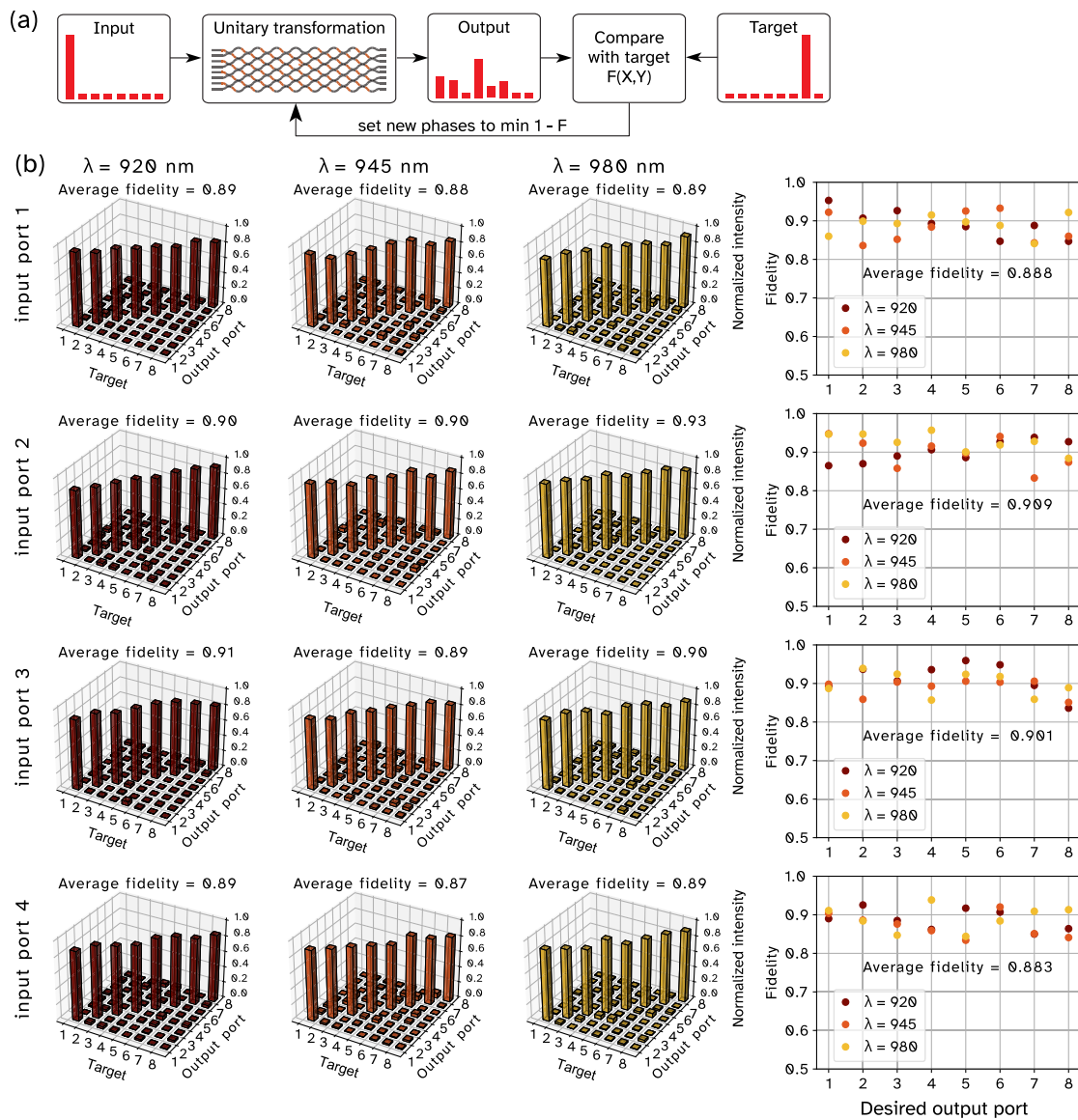


Fig. 6. (a) Illustration of the optimization principle used for programming the interferometer. (b) Results of VFSA optimization of the phaseshifts to realize optical port-to-port switching for three wavelengths: 920, 945, and 980 nm. Histograms of the power distribution in the output ports of the device optimized for 1 to 1 switching to the specific output are shown for each input port and for each wavelength. The fidelity of the observed distribution to the expected one is shown for each input port in the graphs on the right.

registered time for complete reconfiguration of the chip, which included switching phases on all 56 PSs, was no longer than 2 s (see Appendix E for details).

4. DISCUSSION

Even though we have only performed PMI programming in the classical regime, each optimization run still takes several hundred iterations and about 1 h to converge properly. However, once the phase settings for each switching configuration have been established, the PMI does not need to be recalibrated. Unfortunately, the task of programming a PMI with a BS-based architecture, exact BS parameters of which are not precisely known, becomes a black box problem that has no simple analytical solution. Recently, methods were proposed to reconstruct the internal structure of an interferometer using auxiliary measurements [34–36]. These methods apply well-known machine learning techniques to yield the unitary matrices of individual components in the photonic circuit of an interferometer and, as a result, to develop an accurate numerical model of a device under study. This model helps to transfer the optimization task from a real device to a corresponding numerical model, thus greatly simplifying the process of programming the required unitaries in PMIs with complex architectures.

The durability of the reconfigurable optical chip is a vital parameter, as it shows how many cycles the optical chip can perform without malfunction of any of its components such as thermo-optical phaseshifters. If even a single thermo-optical phaseshifter breaks, the PMI will lose the universal reconfiguration feature resulting in the decay of optical chip performance, which will further decrease if the number of broken heaters grows. During the series of optimization experiments, each of 56 PSs was switched no less than 48,000 times and ended up undamaged, which evidences the high level of our PMI durability (see Appendix F for details).

It should be noted that there is room for improvement of the PMIs with our architecture using technological and layout improvements, which have been demonstrated recently. We also observed thermal crosstalk between PSs in transverse direction in our PMI, which was automatically taken into account during the optimization procedure run on chip (see Appendix G for details). The measured electrical power required for 2π phase switching on a single PS was 0.33 W (see Appendix H for details). The thermo-optical phaseshifter power efficiency and the crosstalk can be improved by orders of magnitude by augmenting the structure with the thermal insulation trenches [29]. The slightly more complex FSLW waveguide fabrication process [31] enables lower propagation loss and higher refractive index contrast, which in turn positively affects the miniaturization and further upscaling of the FSLW reconfigurable photonics. This makes us believe that femtosecond direct laser writing will stay a technology of choice for rapid and affordable prototyping.

5. CONCLUSION

We have demonstrated the FSLW-fabricated PMI with the BS-based robust architecture by showing its broadband optical power switching operation. The wavelengths of 920, 945, and 980 nm were selected to highlight the robustness of the

PMI architecture to BS reflectivity variations. Having in mind the application of the PMIs in quantum photonics, in particular, for processing high-dimensional quantum states, the wavelength selection range is advocated by the recent introduction of quantum dot single photon sources to quantum photonics [37] that operate efficiently around 910–940 nm. Since the fabrication of a QD source with a fixed required emission wavelength is still a major technological challenge, the demonstrated PMI can be considered as a reliable photonic platform compatible with the sources generating very different wavelengths. In other words, with the robust architecture there is no need in customizing the PMI to a specific wavelength. Moreover, since our error-tolerant architecture is universal regardless of the interferometer implementation method, further scalability could be propelled by exploiting clever approaches to interferometer reconfigurability on the semiconductor photonic platform [38].

APPENDIX A: FABRICATION PROCESS

The waveguide circuit was written with 515 nm laser pulses (second harmonic of an Avesta Antaus ytterbium fiber femtosecond laser system) with 280 fs duration delivered at 1 MHz repetition rate with 120 nJ pulse energy and linear polarization parallel to the writing direction inside a fused silica glass sample. The laser beam was focused with the aspheric lens (NA = 0.55) 15 μm below the surface of the sample. A 150 μm thick cover glass was placed between the lens and the sample for partial correction of spherical aberrations. A reconfigurable beam expander was used to fill the input aperture of the focusing lens. A high-precision AeroTech FiberGlide3D air-bearing system was used to move the sample at a speed of 0.2 mm/s during the waveguide fabrication process. The microscope images of the written waveguide's cross section and corresponding mode profile are shown in Figs. 7(a)–7(c). The TE mode has slightly

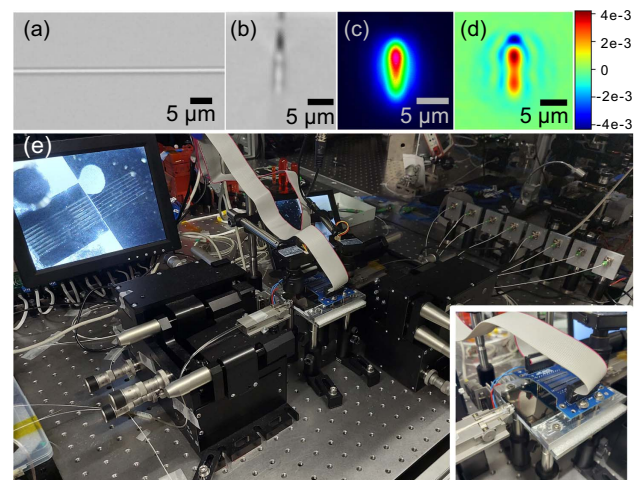


Fig. 7. Microscope images of the (a) top and (b) facet views of the waveguides. (c) Measured TE mode field profile at the 920 nm wavelength. (d) Refractive index contrast profile $\Delta n(x, y)$ reconstructed from the measured near-field waveguide's mode [39,40]. Estimated maximum refractive index change $\Delta n \approx 4 \times 10^{-3}$. (e) Photograph of the experimental setup and optical chip (PMI). Two CCD cameras are used to ease the alignment and visualize the fiber-to-chip and chip-to-fiber coupling at the input and output of the optical chip, respectively.

elliptical nearly Gaussian profile with $1/e^{-2}$ mode field diameters of $5 \mu\text{m} \times 9 \mu\text{m}$ at 920 nm. The refractive index contrast profile $\Delta n(x, y)$ can be reconstructed from the measured near-field intensity distribution of the waveguide's mode [39,40]. The experimental two-dimensional map of the waveguide's refractive index contrast is shown in Fig. 7(d), and the maximum refractive index change is estimated as $\Delta n \approx 4 \times 10^{-3}$. The average propagation loss is 0.6 dB/cm at 910 nm, the coupling loss is 1.5 dB per endface, and the additional bending loss is < 0.1 dB/cm for a 60 mm bending radius used in the experiment.

APPENDIX B: INTERFEROMETER DESIGN

The interferometer design, which includes the waveguide structure and the electrode pattern, is shown in Fig. 8. The radius of curvature is 60 mm for all bends, which is a trade-off between the bending loss effect and the overall size of the waveguide structure achievable using our fabrication technology. The input and output ports are spaced $127 \mu\text{m}$ apart and interfaced with single-mode fiber arrays. The thermo-optical phaseshifters (or electrodes, or heaters) are engraved using the same FSLW setup with a very similar regime to the waveguide writing process. All the FSLW setup parameters for thermo-optical

phaseshifters engraving are identical except for the sample translation velocity, which is five times higher during the electrodes engraving (0.2 mm/s for waveguides writing and 1 mm/s for electrodes engraving) in order to shorten the processing time. The FSLW setup regime for electrodes engraving is less demanding because we only need to remove metal along the electrode border. Certainly, the laser power must be sufficient to engrave the electrode border; however, it should not be too high in order not to damage the surface of the optical chip. Both of these conditions are usually automatically satisfied for the FSLW waveguide writing regime, which is far more difficult to find and may require a separate research [41]. In our fabrication process the thermo-optical phaseshifters are engraved on a thin metallic film, which is sputtered after the waveguide structure of the interferometer has been written. The thermo-optical phaseshifters must be precisely placed exactly above the corresponding waveguides. We ensure the electrode position by exploiting the special markers [blue dots on Fig. 8(a)] previously inscribed underneath the surface in the corners of the fused silica substrate during the waveguide writing process. The thermo-optical phaseshifters are $30 \mu\text{m}$ wide and 2.7 mm long metal stripes, whose shape repeats the corresponding interferometer arm. The transverse (perpendicular to the waveguide axis) spacing between the heaters is $240 \mu\text{m}$.

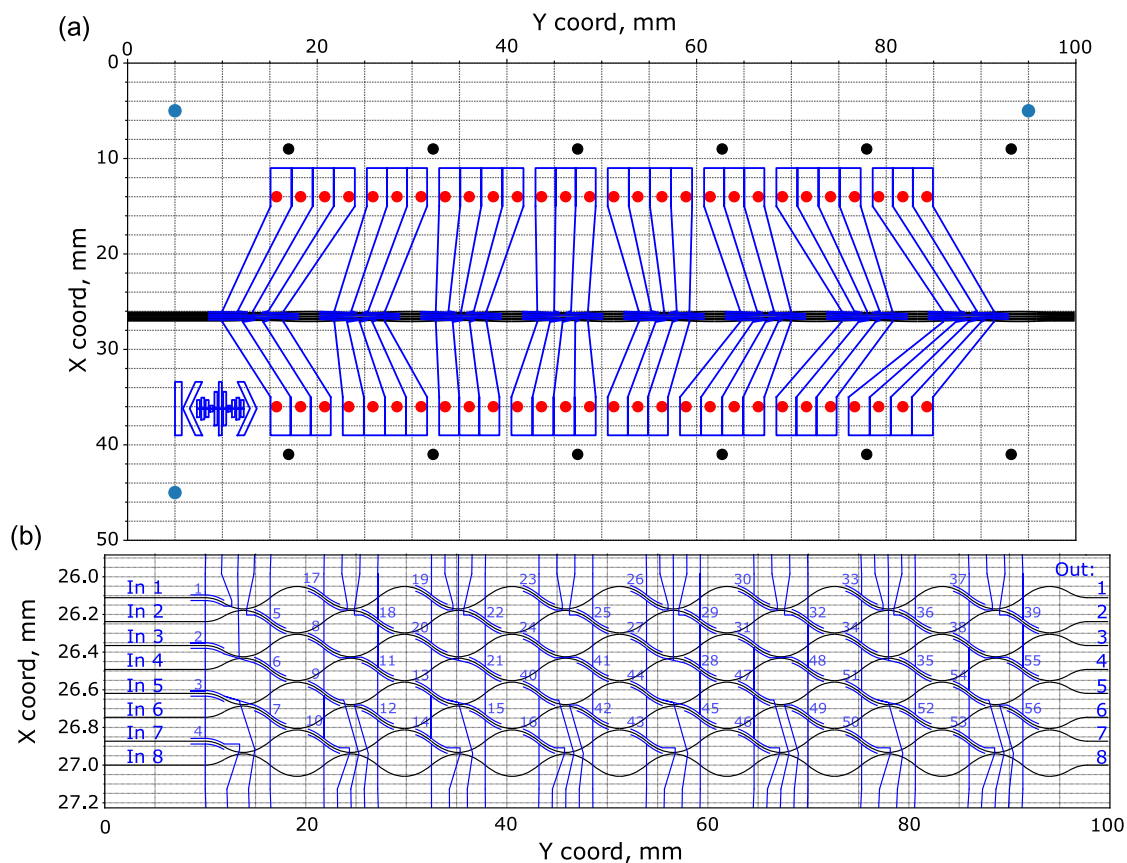


Fig. 8. Actual optical chip structure (view from the top). (a) Real scale scheme of the chip. Red and black dots represent the electrical and ground contacts with the PCB. Blue dots represent special markers on a fused silica sample needed for precise chip alignment before electrodes engraving. (b) Zoomed part of the waveguide structure and electrodes. Waveguides are depicted with black solid lines; engraved electrodes are depicted with blue solid lines. The thin metal film covers all the top surface of the chip—i.e., the whole white area on the figure is conducting—whereas blue lines represent the isolation trenches engraved between the electrodes.

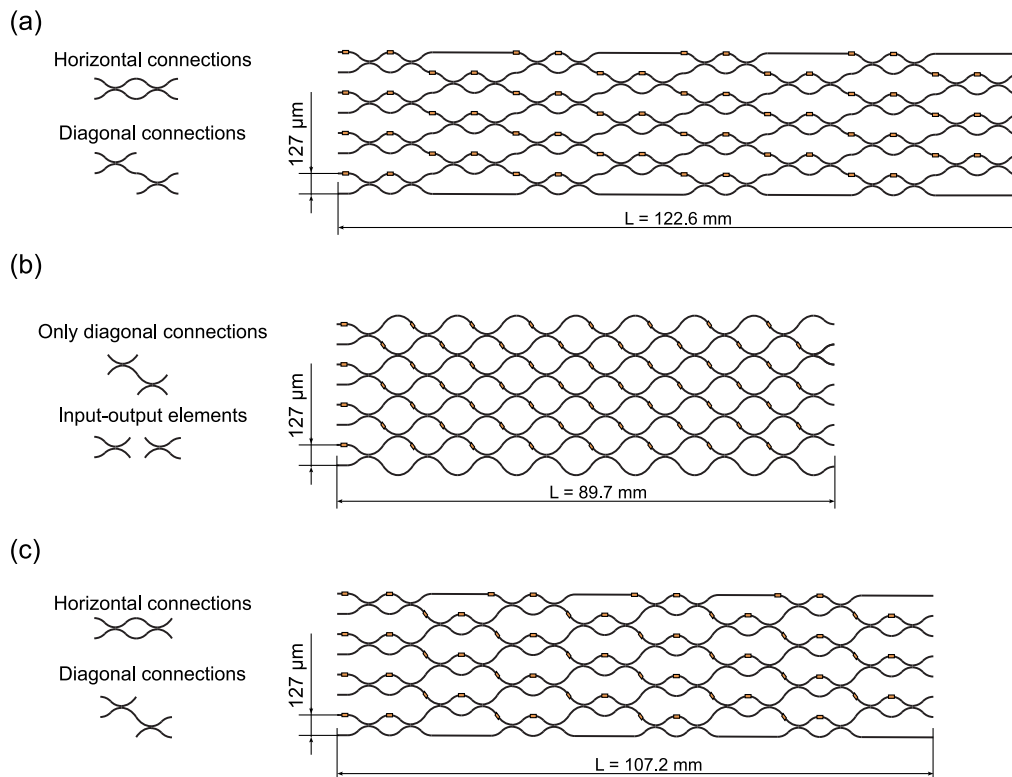


Fig. 9. Comparison of the total lengths of eight-mode interferometers with different architectures with a curvature radius of $R = 60$ mm and an input/output transverse distance between ports equal to $127 \mu\text{m}$. (a) Scheme of an MZI-based interferometer, classic [15] ($L = 122.6$ mm) with straight waveguides connecting individual directional couplers. (b) Scheme of the BS-based error-tolerant interferometer ($L = 89.7$ mm) [19] demonstrated in this work including diagonally connected directional couplers. (c) Scheme of an MZI-based interferometer, hybrid ($L = 107.2$ mm) with optimized directional coupler connections.

The NiCr $0.2 \mu\text{m}$ thick film covers the whole surface of the chip; therefore in Fig. 8 all the white space is covered with metal, while the blue lines represent the engraved tracks, which isolate electrodes from each other. The electrodes are connected to a multichannel digital computer controlled current source via a PCB interface with spring-loaded contacts, whose contact points are schematically shown as red and black dots in Fig. 8(a). (Each red dot corresponds to a single heater, whereas each black dot corresponds to a common round electrode.) The resistances of all heaters fall within the $350\text{--}500 \Omega$ range. The photo of the experimental setup and optical chip is shown in Fig. 7(e).

We also compared the total lengths of eight-mode interferometers with different architectures with a same curvature radius of $R = 60$ mm and a $127 \mu\text{m}$ pitch between input/output ports (see Fig. 9). With these parameters an MZI-based interferometer [15] whose directional couplers are connected to each other with straight waveguide sections has a total circuit length of more than $L = 122$ mm [see Fig. 9(a)]. In contrast, a BS-based error-tolerant interferometer [19] fabricated in this work is shorter by more than 25% and has the total circuit length of less than $L = 90$ mm [see Fig. 9(b)]. This layout has diagonal connections between DCs, which helps to truncate the optical circuit. The error-tolerant interferometer has balanced propagation and bending losses throughout the interferometer. If the straight connections in the MZI-based

interferometer are replaced with diagonal ones [see Fig. 9(c)] the total length shrinks to around 107 mm, which is, however, still more than 15% longer than the BS-based error-tolerant PMI manufactured in this work.

APPENDIX C: NUMERICAL PERFORMANCE COMPARISON WITH MZI-BASED PMI

We have conducted numerical simulations to compare the performance of the port-to-port optical mode switching between our PMI based on error-tolerant architecture [19] and the PMI composed of MZI blocks—conventional universal PMI architecture [15]. In our simulations we tested how inaccuracy in the directional couplers (comprising elements of both PMI architectures) will affect the ability to implement the port-to-port optical mode switching operation that we experimentally performed on our PMI.

We simulated the experiment of port-to-port optical mode switching, as it was held in practice. The transmission coefficients for all the DCs comprising the PMI were varied over a wide range to analyze the performance for a range of wavelengths. The ability to implement port-to-port optical mode switching was tested by running optimizations for each input and output port. If the phaseshift optimization run converged to the infidelity values lower than 10^{-3} for all eight permutations from the input port, then the PMI was considered capable

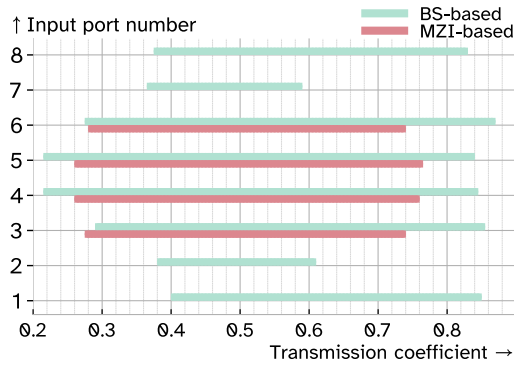


Fig. 10. Simulated numerical comparison of the performance of realizing port-to-port optical mode switching between BS-based error-tolerant PMI [19] and conventional MZI-based PMI [15] architectures. The colored regions show the mean values of normally distributed transmissions of DCs with standard deviation of 0.03 of switching-capable (with infidelity values lower than 10^{-3} for each of eight switchings from the particular input port) PMI configurations.

of realizing the switching; otherwise it was considered incapable. If the PMI with the DC transmission coefficient T (and with a particular input mode) satisfied the criterion, we put a marker on the plot. The results of the numerical simulations are shown in Fig. 5, which proves the higher tolerance to the transmission coefficients of the DCs in the BS-based error-tolerant architecture that we used in our PMI. The colored regions of switching capability are much wider for the BS-based architecture than for the conventional MZI-based PMI architecture [15]. The brightest illustrations of the error tolerance of our architecture are for the input ports 1, 2, 7, and 8, where the MZI-based PMI strictly supported one $T = 0.5$ perfectly balanced DC, while the BS-based PMI architecture has a wide range of available DC transmission coefficients.

Additionally, we performed a similar numerical simulation procedure but for the PMIs, whose DCs' transmission coefficients are distributed normally with mean value T and standard deviation 0.03, which is observed from the experimentally measured transmission coefficients distribution in Fig. 3. The result of this simulation is shown in Fig. 10. The only noteworthy difference from Fig. 5 is the lack of switching capability for the MZI-based PMI for input ports 1, 2, 7, and 8.

APPENDIX D: OPTIMIZATION PROCEDURE AND INFIDELITY CONVERGENCE

We use a modified version of very fast simulated annealing (VFSA) optimization algorithm [33] in our work because it demonstrated slightly faster convergence among other optimization algorithms that we tested (particle swarm and SPSA) for the particular mode switching task in a previously conducted simulation. The magnitudes of the currents running through the phaseshifters were varied as parameters to reproduce the desired optical power distribution between the output ports of the optical chip. Initially all currents were randomly distributed in the range from 0 to 26 mA. At the $(k + 1)$ th iteration of the algorithm, each current was updated according to

$$x_{k+1} = x_k + \alpha y_k (x^{\max} - x^{\min}),$$

where x represents a current on a particular heater (one of 56 heaters); x^{\max} and x^{\min} are bounds for allowed current values (x^{\min} was set to 0, and x^{\max} was set to 26 mA for all heaters), $0 \leq \alpha \leq 1$ is a constant parameter during the whole optimization process controlling the amplitude of step value for currents, and $y_k \in [-1, 1]$ is a stochastic component calculated from

$$y_k = \text{sign}\left(u - \frac{1}{2}\right) T_k [(1 + T_k^{-1})^{2|u-1|} - 1],$$

where u is a real random number uniformly distributed in the interval $[0, 1]$, and T_k is a temperature parameter of the algorithm at the k th step, which decreases according to the cooling schedule:

$$T_k = T_0 \exp(-ck^{\frac{1}{D}}),$$

where T_0 is an initial temperature parameter of the algorithm, c is a parameter of the algorithm defining the speed of temperature T_k descend, and D is a total number of variables of the cost function, which in our case is the total number of heaters $D = 56$.

The algorithm stops after reaching the final temperature, which is also set as a constant algorithm parameter. Alternatively, algorithm can be intentionally interrupted after a particular iteration number. Empirically we found these VFSA parameters to be optimal in terms of the convergence speed: $T_0 = 2$, $\alpha = 0.1$, $c = 4.0$.

The infidelity defined in Eq. (1) is used as a cost function of the distance between the measured (X) and the target (Y) vectors of power values at the output of the error-tolerant PMI. We minimize the infidelity value by varying the currents on all heaters and establish the vector of optimal currents, which implements the required transformation in the PMI. We limited the optimization algorithm to 500 iterations because longer optimization runs did not yield sufficiently better results. We conclude that the nonzero final infidelity values correspond to technological limitations of the interferometer fabrication. Figure 11 shows the infidelity convergence process for each of the four different input ports.

The performance of the device was demonstrated by realizing a specific task—broadband port-to-port optical switching—which implements transfer of the radiation energy from an input port to the chosen output port of the interferometer. However, according to the original proposal [19] the error-tolerant architecture guarantees the possibility to achieve an arbitrary power distribution at the output. As an example we prepared the uniform output power distribution using three different wavelengths, and the distributions that resemble the shape of the Lomonosov Moscow State University's main building (MSU), while input radiation was injected into the first port of the optical chip (see Fig. 12). Optimal currents obtained by the optimization for realizing several switching tasks for the first input port of the optical chip are listed in Table 1, where thermo-optical phaseshifters are numbered according to Fig. 8(b). When radiation is launched into the first input port, the first 16 thermo-optical phaseshifters do not impact the output optical power distribution simply because in

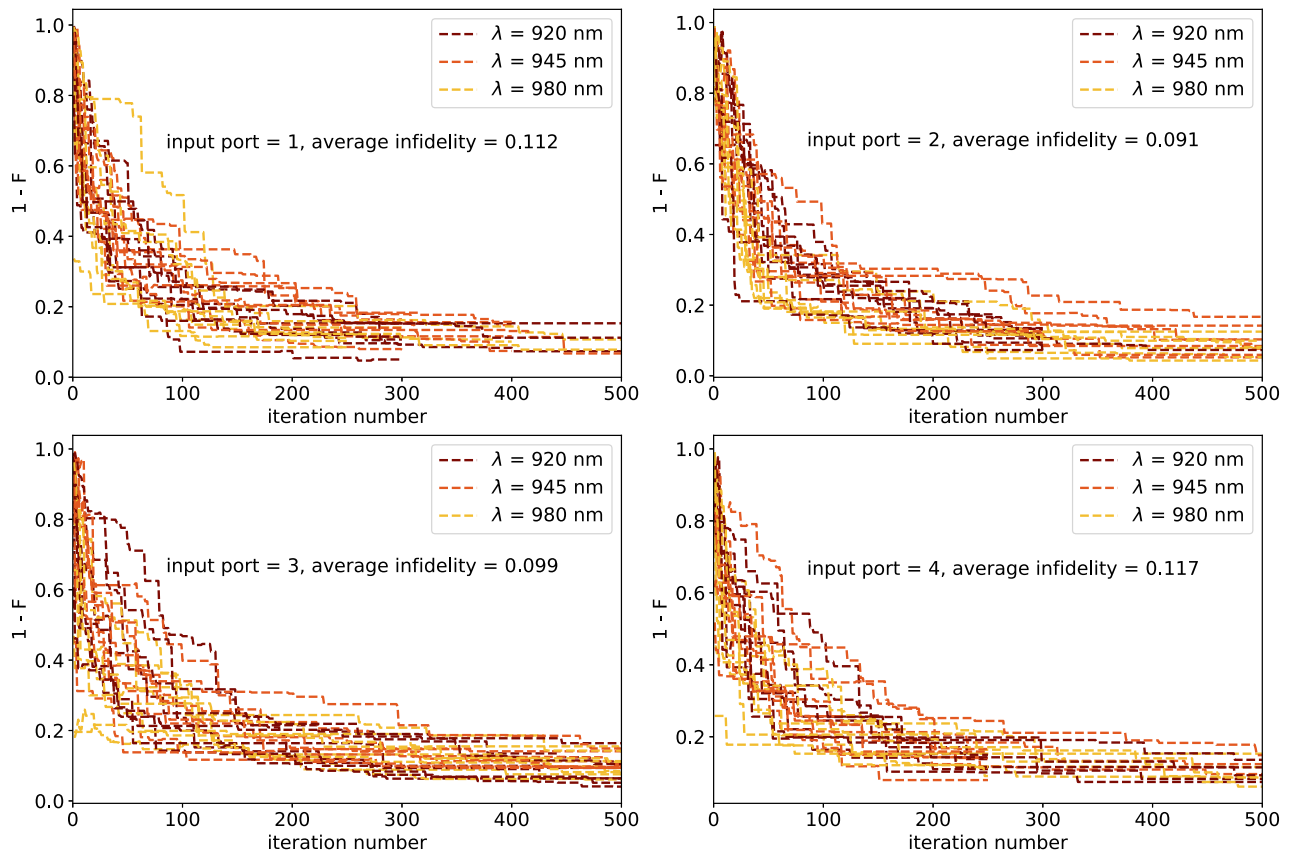


Fig. 11. Convergence of the infidelity value. Each figure contains information about 24 optimizations. These are the results of phaseshift optimizations that minimize the infidelity between the target and measured output vectors. For each of the four first input ports, eight optimization runs were performed to switch all radiation power to any of the output modes using laser light with three different wavelengths (920, 945, and 980 nm).

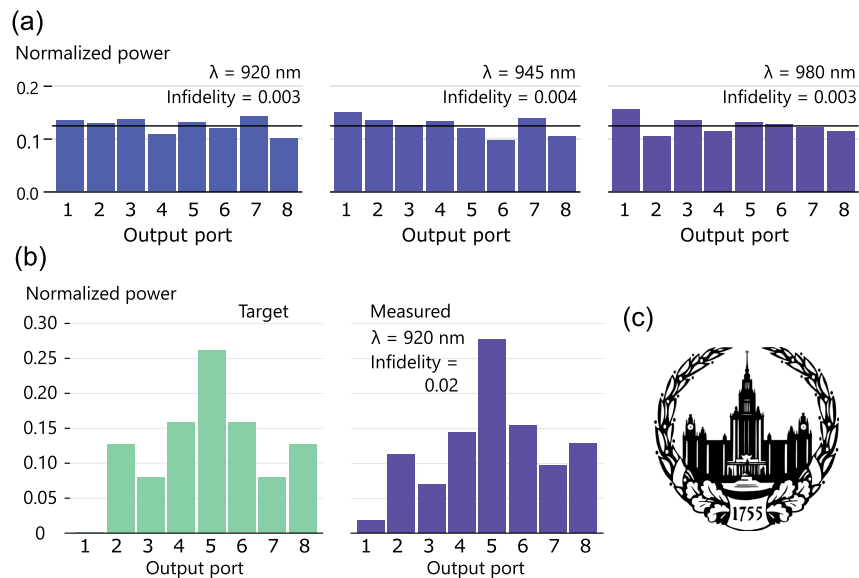


Fig. 12. Examples of achievable output power distributions of the studied optical chip with input radiation injected into the first port. (a) Uniform power distributions obtained using three different laser wavelengths, (b) power distributions replicating the shape of the main building of the Lomonosov Moscow State University (MSU), and (c) logo of the Lomonosov Moscow State University, which illustrates the main building.

Table 1. Optimal Current Values Found by the Optimization Realizing the Particular Switching Task at Given Wavelength^a

Heater No.	Resistance, Ω	Current, mA					
		920 nm 1 to 3	920 nm 1 to 6	920 nm 1 to MSU	920 nm 1 to Uniform	945 nm 1 to Uniform	980 nm 1 to Uniform
17	491	27.96	20.20	24.57	13.48	2.88	14.38
18	448	19.06	6.48	11.68	16.68	13.27	0.97
19	414	16.26	7.41	21.70	22.52	4.81	11.48
20	426	2.80	1.74	1.39	4.05	13.74	18.56
21	409	3.36	14.20	8.42	15.47	0.07	1.57
22	398	0.07	25.68	26.99	23.46	25.37	23.48
23	386	9.67	14.13	3.21	20.71	6.47	16.55
24	400	6.56	20.31	24.69	5.09	4.85	19.12
25	373	17.97	10.89	4.31	4.58	3.08	8.25
26	373	18.07	20.35	16.68	20.10	26.04	12.78
27	386	12.45	14.77	15.11	7.45	14.86	12.26
28	379	18.53	13.98	0.07	4.68	1.03	5.26
29	366	4.88	17.10	0.39	26.27	13.62	5.05
30	365	20.52	16.34	12.62	15.41	13.90	6.99
31	379	8.73	12.44	10.30	6.83	11.54	26.00
32	362	0.89	23.21	15.75	11.99	4.06	5.08
33	382	15.54	0.89	14.79	4.22	8.31	9.58
34	397	14.46	1.88	1.60	2.41	0.57	0.20
35	402	22.79	6.52	9.04	24.22	4.98	0.24
36	383	17.63	11.32	8.59	4.64	18.60	16.39
37	418	21.00	23.23	26.36	1.41	0.07	12.43
38	436	15.82	20.45	3.01	15.40	16.27	19.81
39	462	15.25	7.86	19.50	24.44	15.38	14.19
40	393	13.86	1.75	24.61	25.56	0.56	4.65
41	389	16.22	6.48	18.14	6.65	13.99	8.50
42	378	10.62	21.58	23.46	7.95	17.96	0.47
43	373	4.31	5.72	21.23	4.87	0.07	0.73
44	384	9.70	22.79	21.62	26.25	2.16	22.22
45	362	13.16	15.63	0.69	5.9	18.42	7.12
46	369	22.64	17.05	9.70	9.00	0.07	2.21
47	377	21.09	0.07	17.54	11.18	24.17	5.50
48	374	24.59	25.58	5.05	16.96	4.37	7.74
49	357	8.88	6.53	22.85	10.56	13.10	6.53
50	407	22.62	10.96	5.04	8.97	11.56	14.78
51	389	13.43	11.18	23.96	0.22	6.91	18.31
52	380	11.34	24.72	3.12	5.50	19.36	9.72
53	428	0.85	5.42	3.15	12.18	0.07	0.09
54	439	22.18	21.75	4.55	1.94	9.13	1.37
55	488	15.72	0.47	0.31	8.61	4.39	5.84
56	432	20.56	18.69	1.61	22.77	19.45	3.36
Total Power, W		4.03	3.71	3.64	3.33	2.42	2.26

^aThermo-optical phaseshifters are numbered according to Fig. 8(b). The lowermost row shows the total required amount of electrical power calculated as $\sum R_k I_k^2$.

such a case these phaseshifters control phase delays in interferometer arms without radiation. Therefore, the corresponding 16 heaters were not optimized for the first input port to avoid extra heating of the optical chip. This is the reason that in Table 1 not all 56 heaters are listed. However, if input radiation was distributed among several input ports of the PMI, all 56 heaters would be optimized to achieve the desired output optical power distribution.

APPENDIX E: TIMES OF RECONFIGURATION

We measured typical thermo-optical heater time responses both by applying a π phase on a single heater and by registering the time of complete reconfiguration of the chips' transformation, which implies changing all 56 phaseshifts at a time. The

results are shown in Fig. 13. It can be seen that applying a phaseshift on a single heater takes no longer than 150 ms [see Figs. 13(a)–13(c)], while the full reconfiguration of the optical chip requires up to 1 s due to thermal relaxation processes [see Figs. 13(e) and 13(f)]. In addition, Fig. 13(d) shows the stability of the chips' operation during a complete thermal power redistribution due to the switching from one transformation to another.

APPENDIX F: RECONFIGURABLE OPTICAL CHIP DURABILITY

For our PMI we observe both a high level of performance and durability, which can be estimated by the total number of switching of each heater during the optimization runs

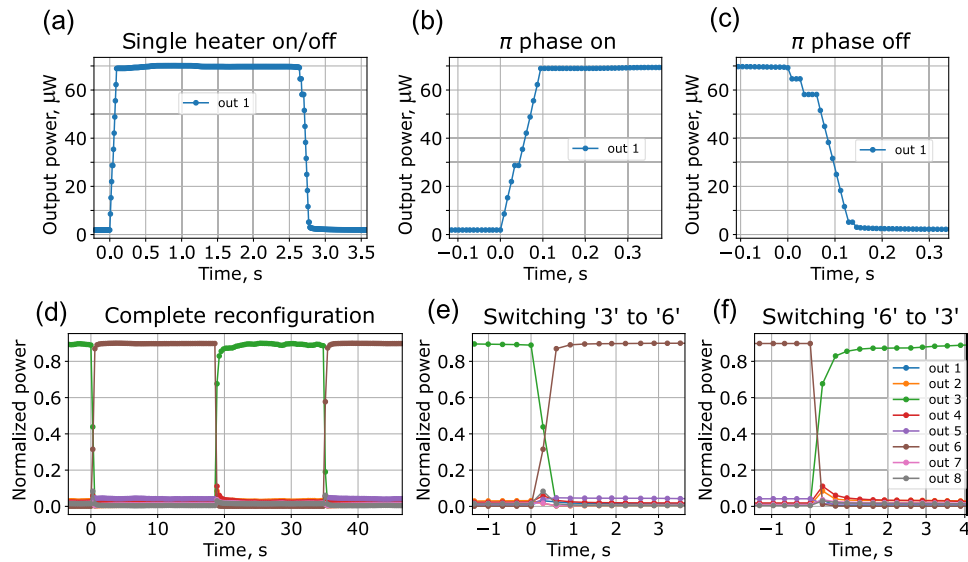


Fig. 13. Measured times of reconfiguration of the fabricated optical chip. (a) Turning on and off the phaseshift π on a single heater. (b) Applying phase π on a single heater takes ≈ 100 ms. (c) Turning the phase π off on a single heater lasts no longer than 150 ms. (d) Switching the chips' transformation from configuration where most of output power exits the third output port to configuration where most of the power exits from the sixth output port and back. (e) Switching from the third output to the sixth output takes ≈ 1 s. (f) Switching from the sixth output to the third output takes ≈ 2 s.

conducted for obtaining the results presented in the main text (see Fig. 6). Total number of optimization runs on the PMI was no less than 96 in order to obtain the main result. Every optimization run on chip contained 500 iterations, where at each optimization step optical chip was reconfigured by applying new currents on all the 56 heaters, which leads to the overall $4 \times 8 \times 3 \times 500 = 48,000$ switches of each heater on the chip and $48,000 \times 56 \approx 2.7$ million heater switches in total. In terms of operating time each optimization step was 10 s long, yielding to $48,000 \times 10(\text{s}) \approx 133$ h of the optical chip being instantly heated. In fact, these estimations are lower bounds on the actual numbers of chips' operations, as, for example, some of the optimizations on chip were launched more than once. All 56 phaseshifters appeared to be undamaged afterwards, which evidences the high level of our PMI durability.

APPENDIX G: HEATER CROSSTALK

We observe the crosstalk effect in the transverse direction in our PMI. We experimentally estimate the strength of a heating crosstalk between two heaters in a column as follows: coherent radiation from a diode laser is injected into the first input mode of the optical chip and electrical current is applied to a single heater—h1, h2, or h3 [see Fig. 14(a)]—and the optical power from all outputs is logged down. Each heater h1, h2, or h3 has resistance of 480Ω . Current was applied in the range from 0 to 28 mA with a 0.13 mA step. Obtained optical power distributions between output modes were then fitted according to a linear power dependence law:

$$P_j = A - B \cos(\alpha x^2 + \phi_0), \quad (\text{G1})$$

where P_j is the normalized optical power from the j th output port; x is the electrical current value; and α , ϕ_0 , A , and B are

the model parameters. The strength of the heater influence is characterized by the α parameter. Therefore, the relation between thermal influences can be estimated as the relation between the corresponding α_{bj} parameters.

The measured normalized output power distributions as a function of the applied electrical current are shown in Fig. 14. The output of the curve fitting algorithm is provided in Table 2, which shows that the crosstalks α_{h2} and α_{h3} are 3.26 and 6.35 times weaker than the direct h1 heater effect α_{h1} .

The presence of the thermal crosstalks between neighboring heaters may complicate the tuning of the PMI because they have to be accounted, for example, in a heater calibration procedure. However, the optimization routine automatically compensates the crosstalk effect and finds an optimal phaseshift configuration corresponding to the chosen transformation.

APPENDIX H: POWER CONSUMPTION

A typical phaseshift from applied electrical current dependence for a single heater with resistance of 480Ω is shown in Fig. 14(a). The current corresponding to 2π phaseshift is equal to 26.1 mA, yielding the 0.33 W of the dissipated thermal energy. Thus, the maximal electrical power applied to the optical chip can be estimated as 18.5 W. The thermoelectric element cooling power used for the PMI temperature stabilization is around 50 W. All the port-to-port optical mode switching configurations presented in the main text (Fig. 6) appeared to consume no more than 5 W of electrical power each. For instance, configurations with the power directed to the third output and to the sixth output displayed in Figs. 13(d)–13(f) require 4.03 W and 3.71 W of electrical power, respectively (see Table 1).

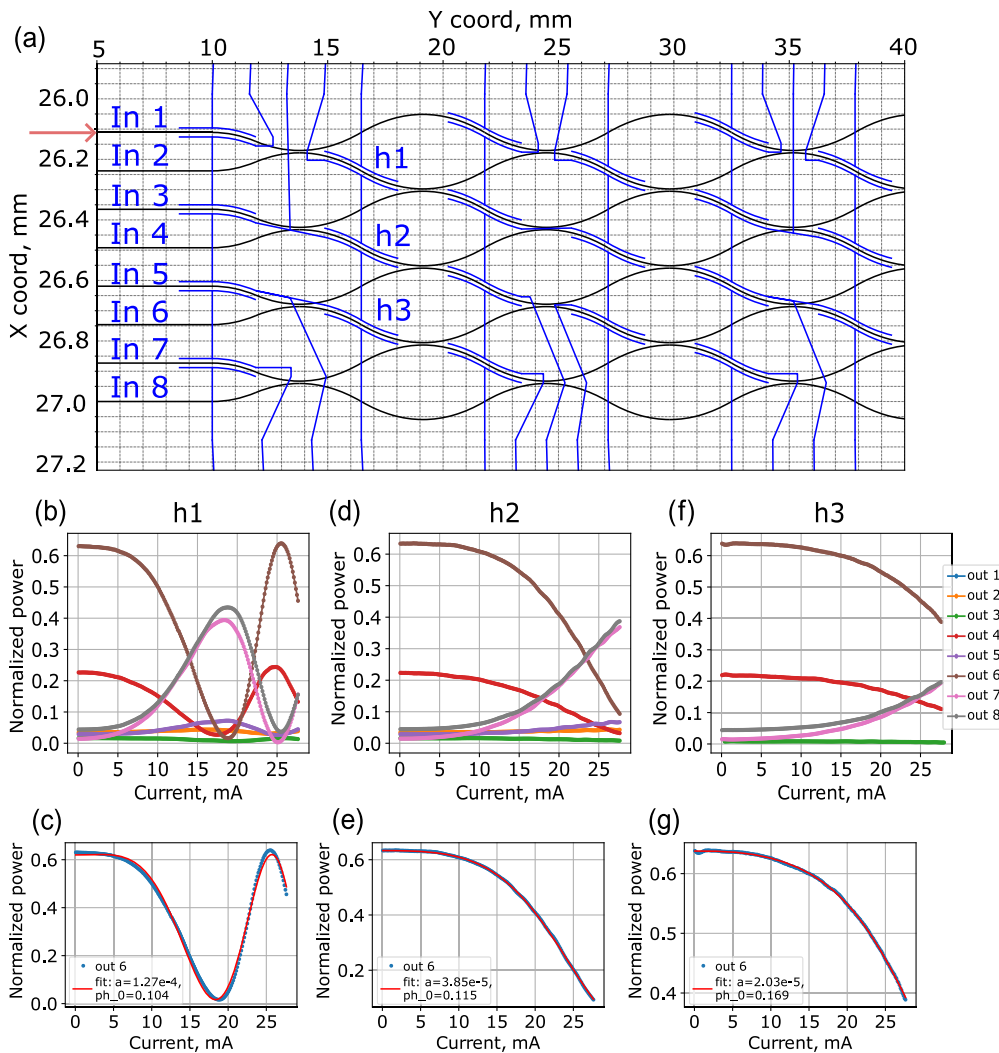


Fig. 14. Measured thermal crosstalk between heaters in the transverse direction. (a) Crosstalk measurement protocol: light was injected into first input mode of the optical chip and electrical current was applied to a single heater (h1, h2, or h3, each with resistance of 480 Ω) in the range from 0 to 28 mA with a 0.13 mA step. (b) and (c) Measured optical power during the current sweep through the heater h1 and the model fit of the data. The current corresponding to 2π phaseshift is equal to 26.1 mA, which yields the 0.33 W of dissipated heat. (d) and (e) Measured optical power during the current sweep through the heater h2 and the model fit of the data. (f) and (g) Measured optical power during the current sweep through the heater h3 and the model fit of the data. The phaseshift induced by a heater is $\phi(x) = \alpha x^2 + \phi_0$, where ϕ is the phase induced by the applied current x and ϕ_0 is the constant phase offset.

Table 2. Fitted Parameters for Three Heaters in One Vertical Column (see Fig. 14) Characterizing the Thermal Crosstalk Effect Acting on the Heater h1^a

Heater	α	ϕ_0	A	B
h1	1.27×10^{-4}	0.104	0.68	0.30
h2	3.85×10^{-5}	0.115	0.68	0.32
h3	2.03×10^{-5}	0.169	0.68	0.32

^aThe α parameter describes the strength of a heater. The induced phaseshift is $\phi(x) = \alpha x^2 + \phi_0$, where ϕ is the phase induced by the current x running through the heater and ϕ_0 is a constant phase offset present even when the driving current is zero.

Funding. State Atomic Energy Corporation ROSATOM (868-1.3-15/15-2021, Roadmap for Quantum computing); Russian Science Foundation (22-12-00353).

Acknowledgment. The work was supported by Rosatom in the framework of the Roadmap for quantum computing in part of the fabrication of integrated photonic chips. The work was supported by RSF [42] in part of the development and experimental assessment of the reconfiguration algorithm.

Disclosures. The authors declare no conflicts of interest.

Data Availability. Data underlying the results presented in this paper are not publicly available at this time but may be obtained from the authors upon reasonable request.

REFERENCES

1. N. C. Harris, J. Carolan, D. Bunandar, *et al.*, "Linear programmable nanophotonic processors," *Optica* **5**, 1623–1631 (2018).

2. D. Pérez, I. Gasulla, and J. Capmany, "Programmable multifunctional integrated nanophotonics," *Nanophotonics* **7**, 1351–1371 (2018).
3. K. Tanizawa, K. Suzuki, M. Toyama, *et al.*, "Ultra-compact 32×32 strictly-non-blocking Si-wire optical switch with fan-out LGA interposer," *Opt. Express* **23**, 17599–17606 (2015).
4. L. Lu, S. Zhao, L. Zhou, *et al.*, " 16×16 non-blocking silicon optical switch based on electro-optic Mach-Zehnder interferometers," *Opt. Express* **24**, 9295–9307 (2016).
5. K. Suzuki, K. Tanizawa, S. Suda, *et al.*, "Broadband silicon photonics 8×8 switch based on double-Mach-Zehnder element switches," *Opt. Express* **25**, 7538–7546 (2017).
6. H. Zhou, J. Dong, J. Cheng, *et al.*, "Photonic matrix multiplication lights up photonic accelerator and beyond," *Light Sci. Appl.* **11**, 30 (2022).
7. J. Cheng, Y. Zhao, W. Zhang, *et al.*, "A small microring array that performs large complex-valued matrix-vector multiplication," *Front. Optoelectron.* **15**, 15 (2022).
8. J. Capmany and D. Pérez, *Programmable Integrated Photonics* (Oxford University, 2020).
9. J. Carolan, C. Harrold, C. Sparrow, *et al.*, "Universal linear optics," *Science* **349**, 711–716 (2015).
10. P. Sibson, C. Erven, M. Godfrey, *et al.*, "Chip-based quantum key distribution," *arXiv*, [arXiv:1509.00768](https://arxiv.org/abs/1509.00768) (2015).
11. Y. Luo, D. Mengu, N. T. Yardimci, *et al.*, "Design of task-specific optical systems using broadband diffractive neural networks," *Light Sci. Appl.* **8**, 112 (2019).
12. A. Goel, C. Tung, Y.-H. Lu, *et al.*, "A survey of methods for low-power deep learning and computer vision," in *IEEE 6th World Forum on Internet of Things (WF-IoT)* (IEEE, 2020), pp. 1–6.
13. A. Peruzzo, J. McClean, P. Shadbolt, *et al.*, "A variational eigenvalue solver on a photonic quantum processor," *Nat. Commun.* **5**, 4213 (2014).
14. M. Reck, A. Zeilinger, H. J. Bernstein, *et al.*, "Experimental realization of any discrete unitary operator," *Phys. Rev. Lett.* **73**, 58–61 (1994).
15. W. R. Clements, P. C. Humphreys, B. J. Metcalf, *et al.*, "Optimal design for universal multiport interferometers," *Optica* **3**, 1460–1465 (2016).
16. S. M. P. Kalaiselvi, E. Tang, H. Moser, *et al.*, "Wafer scale manufacturing of high precision micro-optical components through X-ray lithography yielding 1800 gray levels in a fingertip sized chip," *Sci. Rep.* **12**, 1–12 (2022).
17. M. Y. Saygin, I. V. Kondratyev, I. V. Dyakonov, *et al.*, "Robust architecture for programmable universal unitaries," *Phys. Rev. Lett.* **124**, 010501 (2020).
18. J. Bao, Z. Fu, T. Pramanik, *et al.*, "Very-large-scale integrated quantum graph photonics," *Nat. Photonics* **17**, 573–581 (2023).
19. S. A. Fldzhyan, M. Y. Saygin, and S. P. Kulik, "Optimal design of error-tolerant reprogrammable multiport interferometers," *Opt. Lett.* **45**, 2632–2635 (2020).
20. R. Burgwal, W. R. Clements, D. H. Smith, *et al.*, "Using an imperfect photonic network to implement random unitaries," *Opt. Express* **25**, 28236–28245 (2017).
21. D. A. B. Miller, "Perfect optics with imperfect components," *Optica* **2**, 747–750 (2015).
22. J. W. Silverstone, D. Bonneau, J. L. O'Brien, *et al.*, "Silicon quantum photonics," *IEEE J. Sel. Top. Quantum Electron.* **22**, 390–402 (2016).
23. S. Y. Siew, B. Li, F. Gao, *et al.*, "Review of silicon photonics technology and platform development," *J. Lightwave Technol.* **39**, 4374–4389 (2021).
24. C. Taballione, R. van der Meer, H. J. Snijders, *et al.*, "A 12-mode universal photonic processor for quantum information processing," *Mater. Quantum Technol.* **1**, 035002 (2021).
25. A. Laing and J. L. O'Brien, "Super-stable tomography of any linear optical device," *arXiv*, [arXiv:1208.2868](https://arxiv.org/abs/1208.2868) (2012).
26. R. Tang, R. Tanomura, T. Tanemura, *et al.*, "Ten-port unitary optical processor on a silicon photonic chip," *ACS Photonics* **8**, 2074–2080 (2021).
27. C. Cai and J. Wang, "Femtosecond laser-fabricated photonic chips for optical communications: a review," *Micromachines* **13**, 630 (2022).
28. F. Flamini, L. Magrini, A. S. Rab, *et al.*, "Thermally reconfigurable quantum photonic circuits at telecom wavelength by femtosecond laser micromachining," *Light Sci. Appl.* **4**, e354 (2015).
29. F. Ceccarelli, S. Atzeni, C. Pentangelo, *et al.*, "Low power reconfigurability and reduced crosstalk in integrated photonic circuits fabricated by femtosecond laser micromachining," *Laser Photonics Rev.* **14**, 2000024 (2020).
30. N. Skryabin, I. Kondratyev, I. Dyakonov, *et al.*, "Two-qubit quantum photonic processor manufactured by femtosecond laser writing," *Appl. Phys. Lett.* **122**, 121102 (2023).
31. C. Pentangelo, F. Ceccarelli, S. Piacentini, *et al.*, "Universal photonic processors fabricated by femtosecond laser writing," *Proc. SPIE* **12004**, 120040B (2022).
32. F. Ceccarelli, S. Atzeni, A. Prencipe, *et al.*, "Thermal phase shifters for femtosecond laser written photonic integrated circuits," *J. Lightwave Technol.* **37**, 4275–4281 (2019).
33. M.-T. Vakil-Baghmisheh and A. Navarbafe, "A modified very fast simulated annealing algorithm," in *International Symposium on Telecommunications* (IEEE, 2008), pp. 61–66.
34. S. Kuzmin, I. Dyakonov, and S. Kulik, "Architecture agnostic algorithm for reconfigurable optical interferometer programming," *Opt. Express* **29**, 38429–38440 (2021).
35. B. Bantysh, K. Katamadze, A. Chernyavskiy, *et al.*, "Fast reconstruction of programmable integrated interferometers," *Opt. Express* **31**, 16729–16742 (2023).
36. N. Maring, A. Fyrrillas, M. Pont, *et al.*, "A general-purpose single-photon-based quantum computing platform," *arXiv*, [arXiv:2306.00874](https://arxiv.org/abs/2306.00874) (2023).
37. Y. Arakawa and M. J. Holmes, "Progress in quantum-dot single photon sources for quantum information technologies: a broad spectrum overview," *Appl. Phys. Rev.* **7**, 021309 (2020).
38. T. Wu, M. Menarini, Z. Gao, *et al.*, "Lithography-free reconfigurable integrated photonic processor," *Nat. Photonics* **17**, 710–716 (2023).
39. I. Mansour and F. Caccavale, "An improved procedure to calculate the refractive index profile from the measured near-field intensity," *J. Lightwave Technol.* **14**, 423–428 (1996).
40. S. Wu, Z. Gao, T. Wu, *et al.*, "Ultrafast heterodyne mode imaging and refractive index mapping of a femtosecond laser written multimode waveguide," *Opt. Lett.* **47**, 214–217 (2022).
41. A. Abou Khalil, P. Lalanne, J.-P. Bérubé, *et al.*, "Femtosecond laser writing of near-surface waveguides for refractive-index sensing," *Opt. Express* **27**, 31130–31143 (2019).
42. <https://rscf.ru/en/project/22-12-00353/>.